# Transitions in Poiseuille flow of nematic liquid crystal

T.G. Anderson [1], E. Mema, L. Kondic, L.J. Cummings *

Department of Mathematical Sciences, New Jersey Institute of Technology, Newark, NJ 07102-1982, United States

A B S T R A C T

Recent experiments by Sengupta et al. (Phys. Rev. Lett. 2013) [9] revealed interesting transitions that can occur in flow of nematic liquid crystal under carefully controlled conditions within a long microfluidic channel of width much larger than height, and homeotropic anchoring at the walls. At low flow rates the director field of the nematic adopts a configuration that is dominated by the surface anchoring, being nearly parallel to the channel height direction over most of the cross-section; but at high flow rates there is a transition to a flow-dominated state, where the director configuration at the channel centerline is aligned with the flow (perpendicular to the channel height direction). We analyze simple channel-flow solutions to the Leslie–Ericksen model for nematics. We demonstrate that two solutions exist, at all flow rates, but that there is a transition between the elastic free energies of these solutions: the anchoring-dominated solution has the lowest energy at low flow rates, and the flow-dominated solution has lowest energy at high flow rates.

© 2015 Elsevier Ltd. All rights reserved.

## 1. Introduction

Sengupta and co-workers [9] recently carried out careful experiments with nematic liquid crystal (NLC) in a microfluidic of rectangular cross-section. A variety of imaging techniques (polarizing optical microscopy, fluorescence confocal polarizing microscopy, particle tracking velocimetry) was used to visualize both the molecular orientation (director configuration) within the NLC, and the velocity profile, across the microfluidic channel height. The experimental observations revealed intriguing transitions in the director field of the NLC as the flow rate was varied, between an "anchoring dominated" state at low flow rates, and a "flow-dominated" state at high flow rates, as we explain below.

The experiments carried out were all in the regime where the aspect ratio of the rectangular cross-section was small: height $2h$ much smaller than width $2w$, with both in turn much smaller than the channel length in the flow direction.[2] Nematic anchoring at all channel walls was homeotropic (molecules aligning perpendicular to the walls). Throughout this paper we will identify coordinate directions as follows: $x$ aligned with the channel length, $y$ with the channel width, and $z$ with the channel height, so that the channel cross-section is $|y| \leq w$, $|z| \leq h$. In the absence of flow, the director assumes a configuration that is aligned with the $z$-direction over

most of the channel, respecting the anchoring at the walls $z = \pm h$ (except near the side walls $y = \pm w$ where it adjusts to the anchoring at those walls). At low flow rates the director is only moderately perturbed from this state by the flow, and is again aligned with the $z$-direction across the channel centerline $y = z = 0$ (the $x$-axis). At high flow rates however, imaging reveals the director field to be aligned with the flow ($x$-direction) at the channel centerline, while still respecting the homeotropic anchoring at the channel walls $z = \pm h$. At intermediate flow rates more complex flow regimes are observed, where the director adopts a fully three-dimensional configuration; but over much of the range of flow rates studied flow is nearly two-dimensional, having little variation in the $y$-direction.

The experiments were complemented by numerical modeling of the experimental setup, using the $Q$-tensor approach [9], with a Lattice-Boltzmann algorithm to compute the steady state flow and director field. No slip and strong homeotropic anchoring conditions were imposed on the channel walls. Such three-dimensional simulations are computationally intensive however, and provide only limited analytical insight into the flow and its transitions. The purpose of this note is to investigate the simplest model system that can exhibit such transitions: two-dimensional Poiseuille flow in a parallel-sided channel, using the Leslie–Ericksen formalism for nematodynamics. We show that, at all flow rates, two exact solutions to the flow problem exist, which we identify with the weak flow and strong flow regimes in the experiments. The elastic free energies of these two solutions are readily computed as a function of the applied pressure gradient, which correlates directly with the flow rate. We show that there is a critical pressure gradient at which the energies cross over, which we identify with

the transition between the weak and strong flow experimental regimes. With strong homeotropic anchoring at the boundaries the predicted transition occurs at a significantly higher flow rate than in the experiments. However, introducing finite anchoring strength at the channel walls can lower the transition point to that observed experimentally.

## 2. Mathematical model

We use the Leslie–Ericksen model for flow of nematic liquid crystals (NLCs) [7] and consider the idealized problem of steady, two-dimensional, unidirectional channel flow, with homeotropic anchoring conditions at the channel walls and symmetry about the channel centerline. We seek solutions for the velocity $\mathbf{v}$ and director field $\mathbf{n}$ of the form $\mathbf{v} = (u(z), 0, 0)$ and $\mathbf{n} = (\sin \theta(z), 0, \cos \theta(z))$ in a channel $-h \leq z \leq h$. The full governing equations are given in Appendix A. In addition to our restriction to simple unidirectional flow we make the common assumption that the NLC has equal elastic constants, all being equal to a single elastic constant $K$ [2,3,11].

Substituting the assumed forms for $\mathbf{v}$, $\mathbf{n}$ into Eqs. (12)–(14) we obtain, after integration, simplification, and use of the symmetry about the channel centerline,

$$\frac{du}{dz} = -\frac{2K\theta''(z)}{\gamma_1 - \gamma_2 \cos 2\theta} \tag{1}$$

$$\frac{K\theta''(z)}{\gamma_1 - \gamma_2 \cos 2\theta} \left\{ \alpha_1 \sin^2 \theta \cos^2 \theta + \frac{\alpha_5 - \alpha_2}{2} \cos^2 \theta + \frac{\alpha_3 + \alpha_6}{2} \sin^2 \theta + \frac{\alpha_4}{2} \right\} = \frac{Gz}{2} \tag{2}$$

where $\gamma_1 = \alpha_3 - \alpha_2$, $\gamma_2 = \alpha_6 - \alpha_5$, the $\alpha_i$ are constant viscosities for the NLC (see Appendix A), and $(-G)$ is the pressure gradient in the channel.

Motivated by the experimental observations we seek multiple solution branches to these equations, considering first the case where the (homeotropic) anchoring at the channel walls is strong, that is,

$$\theta(h) = 0, \quad \theta(-h) = 0, -\pi. \tag{3}$$

In line with the experimental observations, the second boundary condition here (on $z = -h$) allows us to seek both the "weak flow" solutions (in which the director is only weakly perturbed from the homeotropic anchoring at $z = h$ and therefore respects the same boundary condition at $z = -h$, $\theta(-h) = 0$), and the "strong flow" solutions (in which the director aligns with the flow at the centerline, undergoes a full rotation through angle $(-\pi)$, and therefore satisfies $\theta(-h) = -\pi$). We also subsequently consider the case of weak homeotropic anchoring at both channel walls. Here, using the well-known Rapini–Papoular weak anchoring energy [8] leads to alternative boundary conditions for the director

$$K\frac{d\theta}{dz}\Big|_{z = \pm h} \pm \frac{A}{2} \sin 2\theta(\pm h) = 0, \tag{4}$$

which may be applied instead of (3), where $A$ is the surface anchoring strength.

We solve Eqs. (1), (2) on the channel $-h \leq z \leq h$, imposing also a no-slip boundary condition on the velocity at the upper channel wall, $u(h) = 0$,[3] in addition to the appropriate conditions on $\theta(\pm h)$ (Eqs. (3) or (4)). We seek both weak and strong flow solution branches, as characterized by the different boundary conditions described above. Given the experimental observations, we anticipate the former to be valid in the low flow regime, while the latter should be valid at high flow rates. We note that within the limitations of our steady-state model, mere existence of a solution

is not enough to tell us whether it is experimentally observable: stability analysis, not carried out here, would tell us in which regimes each solution branch is stable. Furthermore, even in parameter regimes where two stable steady states may exist, their respective energies may dictate which solution is seen in practice. We say more about this in Section 3, where we propose an energetics argument to explain the observed flow transitions.

We want to relate our model to the experimental results of Sengupta et al. [9]; however this reference specifies the mean flow speed $\overline{u}$, and not the pressure gradient $(-G)$ that arises naturally in the model. To find a simple heuristic relation between $G$ and $\overline{u}$ we consider the solution for Newtonian Poiseuille flow with viscosity $\mu$ and pressure gradient $(-G)$ in the channel,

$$u = \frac{G}{2\mu}(h^2 - z^2) \quad \text{and} \quad \overline{u} = \frac{1}{2h}\int_{-h}^{h} u \, dz = \frac{Gh^2}{3\mu}.$$

Identifying $\mu$ with the nematic equivalent $\alpha_4/2$, this gives $G = 3\overline{u}\alpha_4/(2h^2)$.

Before solving we non-dimensionalize the equations, scaling lengths with the channel half-width $h$, the velocity $u$ with $\overline{u} = 2Gh^2/(3\alpha_4)$, and all viscosities $\gamma_i, \alpha_i$ with $\alpha_4$. The dimensionless form of the governing equations (1), (2) then becomes, after some manipulation,

$$\frac{du}{dz} = -\frac{3z}{\left\{ 2\alpha_1 \sin^2 \theta \cos^2 \theta + (\alpha_5 - \alpha_2) \cos^2 \theta + (\alpha_3 + \alpha_6) \sin^2 \theta + 1 \right\}} \tag{5}$$

$$\frac{\theta''(z)}{\gamma_1} - \gamma_2 \cos 2\theta \left\{ 2\alpha_1 \sin^2 \theta \cos^2 \theta + (\alpha_5 - \alpha_2) \cos^2 \theta + (\alpha_3 + \alpha_6) \sin^2 \theta + 1 \right\} = \mathcal{G}z \tag{6}$$

where

$$\mathcal{G} = \frac{Gh^3}{K} \tag{7}$$

is a dimensionless pressure gradient. The boundary conditions are

$$u(1) = 0, \quad \theta(1) = 0, \quad \begin{cases} \theta(-1) = 0 & \text{"weak flow" solution} \\ \theta(-1) = -\pi & \text{"strong flow" solution} \end{cases} \tag{8}$$
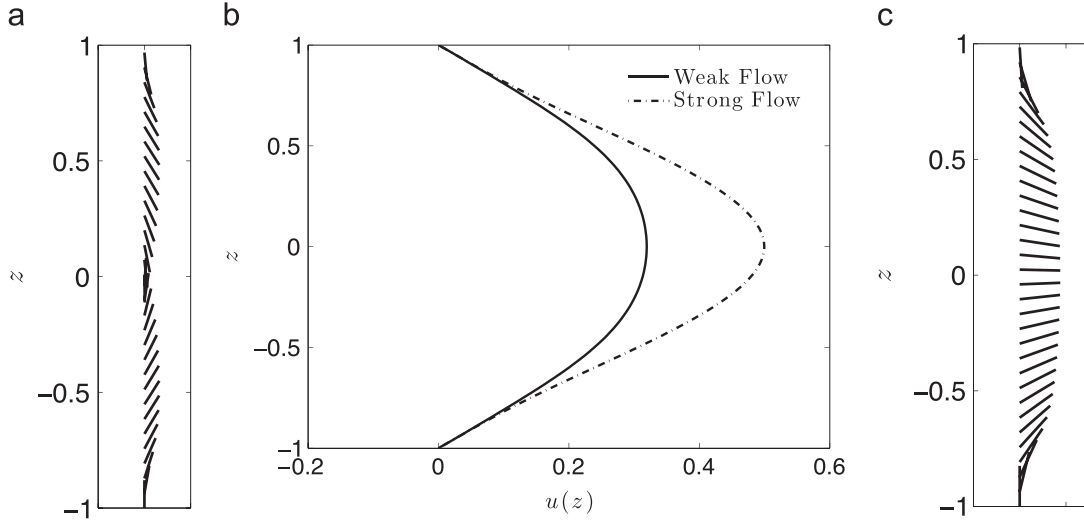
in the strong anchoring case, and

$$u(1) = 0, \quad \frac{d\theta}{dz}\Big|_{z=1} + \mathcal{A}\sin(2\theta(1)) = 0, \quad \frac{d\theta}{dz}\Big|_{z=-1} - \mathcal{A}\sin(2\theta(-1)) = 0, \tag{9}$$

in the weak anchoring case (both solution types), where $\mathcal{A} = Ah/(2K)$ is a dimensionless anchoring strength, and our terminology for the solution types anticipates our findings regarding which solutions to expect in different flow regimes.

We use numerical continuation in $\mathcal{G}$ to track the solution branches as far as possible, starting from $\mathcal{G} = 0$. To initiate the search for the two solution branches, for the weak flow solutions we use an initial guess of $\theta(z) \equiv 0$ at $\mathcal{G} = 0$, and for the strong flow solution branch we use an initial guess of $\theta(z) = (z-1)\pi/2$ at $\mathcal{G} = 0$.

## 3. Results

We compute solutions of the system comprising Eqs. (5)–(8) (strong anchoring), or Eqs. (5)–(7) and (9) (weak anchoring), as the dimensionless pressure gradient parameter $\mathcal{G}$ varies, using parameter values for the liquid crystal 5CB (used by Sengupta et al. [9]) in the nematic state at 27 °C. The values for the dimensionless viscosities are $\alpha_1 = -0.1549$, $\alpha_2 = -0.9859$, $\alpha_3 = -0.0535$, $\alpha_5 = 0.7324$, $\alpha_6 = -0.3944$ (see Appendix B); and $\gamma_1 = \alpha_3 - \alpha_2$, $\gamma_2 = \alpha_6 - \alpha_5$. We find (numerically) that both weak and strong flow

---

[3] Symmetry about the centerline was used in deriving Eqs. (1), (2), so that the no-slip condition on $z = -h$ is satisfied automatically.

**Fig. 1.** (a) Weak flow (anchoring-dominated) director profile across the dimensionless channel width $-1 \leq z \leq 1$; (b) velocity profiles of the two solutions across the channel; (c) strong flow solution across the channel. In all cases anchoring is strong and $\mathcal{G} = 25$ (so that our theory would predict the weak flow solution (a); see Fig. 2).

solution types exist at all $\mathcal{G}$–values. The two solution branches are tracked using simple continuation in the parameter $\mathcal{G}$ (both forward and backward continuation was carried out, with identical results).

Fig. 1 shows typical strong anchoring solutions (boundary conditions (8)), for both director field and velocity profile. We see that the anchoring-dominated (or weak flow) solution in Fig. 1(a) has two regions, symmetrically placed about the channel centerline, within which the director aligns partially with the flow. Near the walls (and also at the channel center-line, by symmetry) the director respects the strong home-otropic anchoring. The velocity profile associated with this solution, Fig. 1(b), is approximately parabolic, but rather blunt. By contrast, the director profile for the flow-dominated solution (Fig. 1(c)) is mostly aligned with the flow, respecting the homeotropic anchoring only near the channel walls. The asso-ciated velocity profile is much sharper than that for the anchoring-dominated solution. These observations on the velo-city profiles are broadly in agreement with the experimental observations; see Fig. 3 of [9]. It is notable that though the two solutions in Fig. 1 are associated with the same pressure gradient, the velocity for the flow-dominated solution is every-where larger than that for the anchoring-dominated solution, the director configuration affording less resistance to the flow.

Since both solutions exist for all flow rates it is not clear which to expect in a given situation. To attempt to answer this we plot the elastic energies of the two solutions, as defined by Eq. (15) in Appendix A, as a function of the dimensionless pressure gradient $\mathcal{G}$. Within our simple model setup the elastic energy is given by $(K/2) \int_{-h}^{h} \theta_z^2 \, dz$. Scaling this energy with the natural scaling $K/h$ we can compare the dimensionless energies of the solutions,

$$\mathcal{E} = \frac{1}{2} \int_{-1}^{1} \theta_z^2 \, dz. \tag{10}$$

The result is shown in Fig. 2: at low values of $\mathcal{G}$ the anchoring-dominated (or weak flow) solution has the lower energy, but for $\mathcal{G} > \mathcal{G}^* \approx 43$, the flow-dominated solution has the lower energy. Therefore, one would expect that for $\mathcal{G} < \mathcal{G}^*$ the anchoring-dominated or weak flow solution would be observed, while for $\mathcal{G} > \mathcal{G}^*$ the strong flow solution would be seen in the experiments.

Before comparing our results to the experimental data, we first consider briefly the influence of weak anchoring on solutions, using boundary conditions (9) instead of (8). We again find (numerically, using continuation in $\mathcal{G}$) that both weak and strong flow solutions exist at all $\mathcal{G}$-values; but the effect of the weak anchoring is to lower
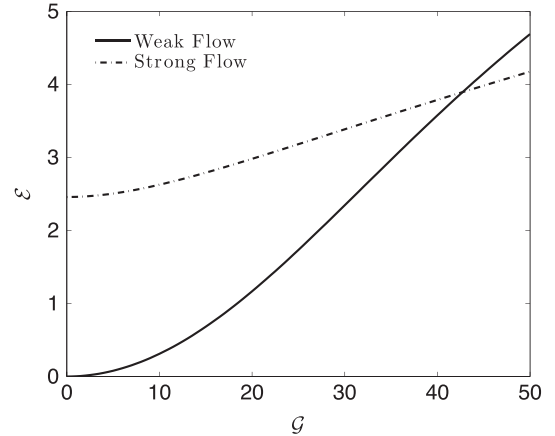


**Fig. 2.** Free energies of the two solutions with strong anchoring as the dimension-less pressure gradient $\mathcal{G}$ is increased.

the critical value $\mathcal{G}^*$ at which the transition in elastic energies occurs. Fig. 3 shows the elastic energies of weak and strong flow solutions when the dimensionless surface energy parameter $\mathcal{A} = 20$ and $\mathcal{A} = 1$: in the former case $\mathcal{G}^* \approx 38$, and in the latter $\mathcal{G}^* \approx 8.5$, compared with $\mathcal{G}^* \approx 43$ in the strong anchoring case ($\mathcal{A} \to \infty$).

Fig. 4 shows the solutions corresponding to these two values of the surface energy $\mathcal{A}$: solutions with $\mathcal{A} = 20$ (shown in (a)–(c)) are not strongly perturbed from the strong anchoring case of Fig. 1, but in the solutions with $\mathcal{A} = 1$ the weak anchoring is evident. For all simulations in Fig. 4 the pressure gradient $\mathcal{G} = 25$ so that, referring to Fig. 3, one would expect the weak flow solution to be observed with $\mathcal{A} = 20$, but the strong flow solution with $\mathcal{A} = 1$.

Fig. 5 shows further how the value of $\mathcal{G}^*$ depends on the surface anchoring parameter $\mathcal{A}$ for the liquid crystal 5CB. The figure reveals how, at large surface energies, the value of $\mathcal{G}^*$ asymptotes to the strong anchoring case considered first, while as $\mathcal{A}$ decreases the value of $\mathcal{G}^*$ decreases abruptly to zero. This is discussed further below.

### 3.1. Comparison to the experiments

A direct comparison with the experimental data of Sengupta et al. [9] requires data on the viscosities for 5CB (given at the start of Section 3 and Appendix B), the elastic constants of 5CB, and also the channel dimensions and the flow rates used in the experiments. The elastic constants for 5CB are approximately $K_1 = 4 \times 10^{-12}$ N
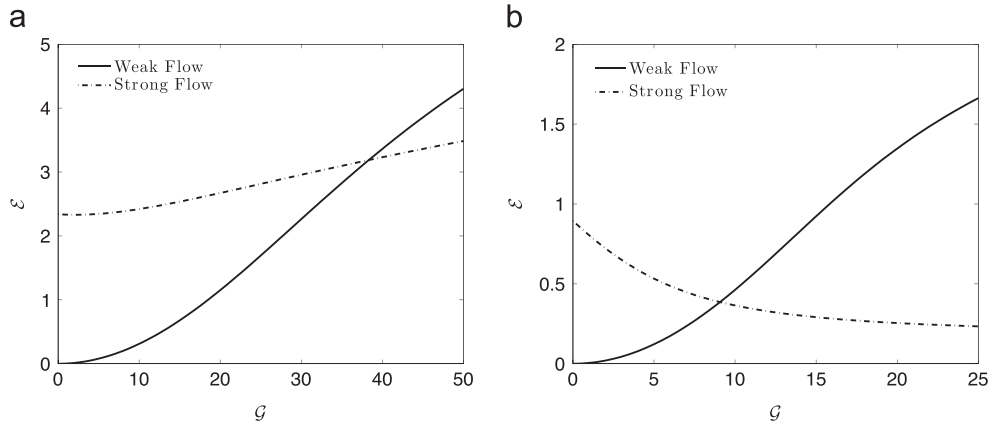
**Fig. 3.** Elastic free energies of the two solutions with weak anchoring boundary conditions: (a) $\mathcal{A} = 20$, showing that the anchoring-dominated (weak flow) solution is anticipated for $\mathcal{G} < \mathcal{G}^* \approx 38$, but the flow-dominated (strong flow) solution is expected at high flow rates $\mathcal{G} > \mathcal{G}^* \approx 38$; (b) $\mathcal{A} = 1$, where similar observations hold, but $\mathcal{G}^*$ has been reduced to a value between 8 and 9.
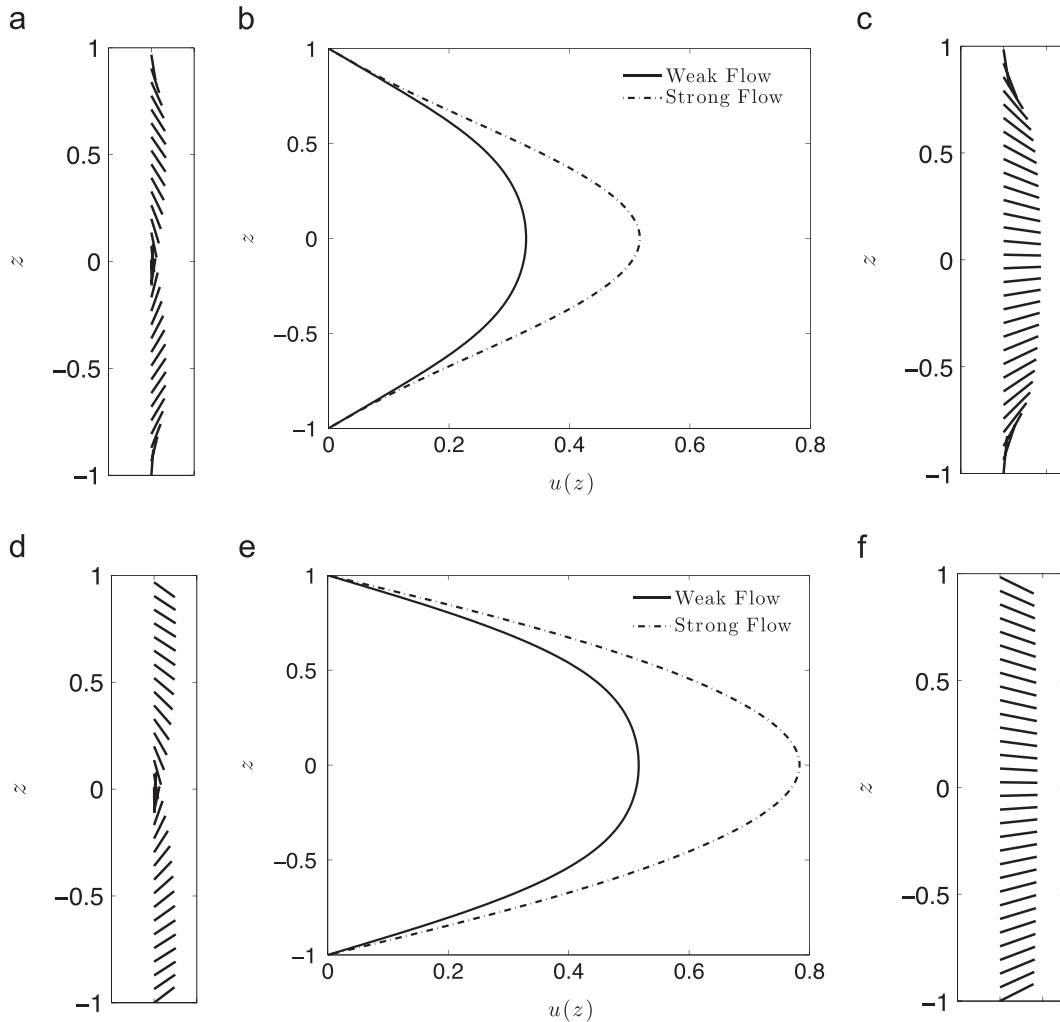


**Fig. 4.** (a)–(c): Director and flow profiles within the channel for moderate anchoring $\mathcal{A} = 20$: (a) weak flow director profile across the dimensionless channel width $-1 \le z \le 1$; (b) velocity profiles of the two solutions; (c) strong flow solution. (d)–(f): Director and flow profiles within the channel for weak anchoring $\mathcal{A} = 1$: (d) weak flow director profile across the dimensionless channel width $-1 \le z \le 1$; (e) velocity profiles of the two solutions; (f) strong flow solution. In all cases $\mathcal{G} = 25$, so that our theory would predict the weak flow solution (a) with $\mathcal{A} = 20$, and the strong flow solution (f) with $\mathcal{A} = 1$; see Fig. 3).

(splay) and $K_3 = 4.8 \times 10^{-12}$ N (bend) (see Appendix B; there is no twist in our two-dimensional problem). Hence our one-constant approximation is quite reasonable, and for this approximation we take the average of these values, $K = 4.4 \times 10^{-12}$ N. The channel
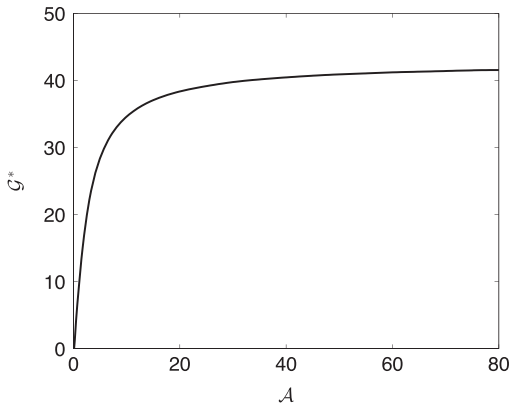
height $2h$ ranges from 7 to 35 μm in the experiments, but the main set of experimental images reported (Fig. 2 in [9]) has $2h = 16$ μm, and the transition from low to high flow director topology is reported to occur for some flow speed $\bar{u}$ between 11 and

100 μm s$^{-1}$. Using our estimate $\bar{u} = 2Gh^2/(3\alpha_4)$ and recalling that $\mathcal{G} = Gh^3/K$ (Eq. (7)), we obtain

$$\mathcal{G} \approx \frac{3\alpha_4 \bar{u} h}{2K}. \tag{11}$$

These considerations indicate that for the nematic liquid crystal 5CB we should see the transition occurring for some value of $\mathcal{G}$ (corresponding to the range of $\bar{u}$-values given above) in the range $(\mathcal{G}^*_{\text{low}}, \mathcal{G}^*_{\text{high}}) = (2.2, 19.4)$. We see that our strong anchoring prediction for the transition point, $\mathcal{G}^* \approx 43$, lies outside this range. Nonetheless, given the simplicity of our model, the prediction it makes is not at all bad.

The introduction of weak anchoring boundary conditions at the channel walls can bring the transition value $\mathcal{G}^*$ down into the experimentally observed range. As can be seen from Fig. 5, a value $\mathcal{A} = 2$ (for example) corresponding to the surface energy $A = 2K\mathcal{A}/h = 2.2 \times 10^{-6}$ N m$^{-1}$ is sufficient for this purpose; and the value $\mathcal{A} = 1$ presented in Figs. 3 and 4 brings $\mathcal{G}^*$ well within the experimental range. Values $\mathcal{A}$ in the range 1–2 are rather small, since typically an order of magnitude larger surface energies are expected (see, e.g. [1]). However, this remark is somewhat speculative, since the authors do not provide details of the true anchor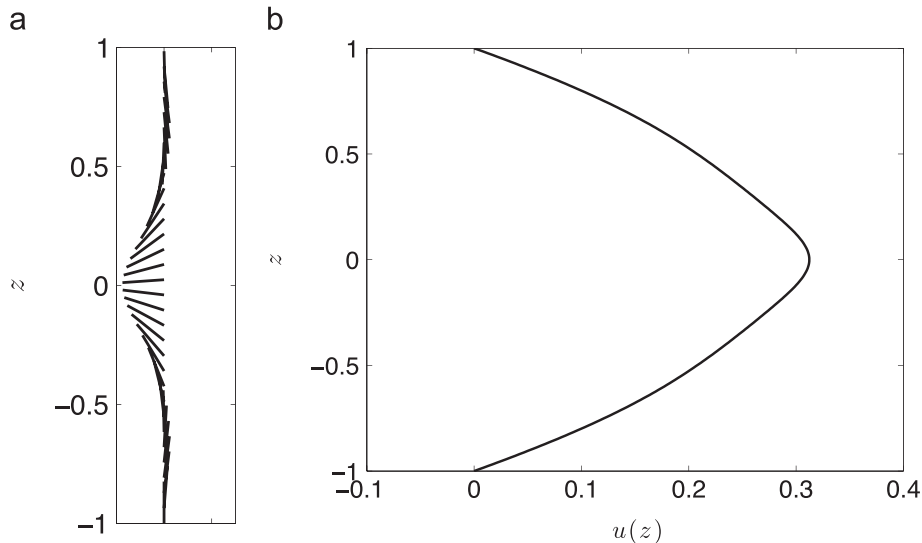ing strength in the experiments. Therefore, while weak anchoring may play some role in explaining the difference between the strong anchoring model predictions and the experimental data, it is unclear whether it is a dominant factor.

## 4. Discussion

The discrepancy between our simple model and the experimental observations could be due to several different factors, possibly acting in combination. Firstly, as already noted, although the experiments were carried out in a microfluidic setup where the channel dimensions were all well-separated, three-dimensional flow effects are undeniably present, especially near transition. Our model assumes a perfectly two-dimensional flow and director field, and can therefore in no way account for such three-dimensional effects. Secondly, the one-constant approximation used, while reasonable, is not quantitatively correct. In some systems it has been demonstrated that the observed director configurations may be rather sensitive to differences in these elastic constants [4].

Thirdly, also noted earlier, our steady-state model (while sound) can say nothing about the stability of steady states that are found to exist. Although we present a possible criterion for flow transitions based on energetic arguments by computing the value $\mathcal{G}^*$ at which the energies of the two steady states cross over, it is possible that the weak flow solution loses stability at some value $\mathcal{G}_{w,s} < \mathcal{G}^*$, so that as $\mathcal{G}$ increases through $\mathcal{G}_{w,s}$ while in the weak flow state, the system has no alternative but to transition to the strong flow state (assuming, of course, that the strong flow state exists and is stable for such $\mathcal{G}$). Conversely of course, if $\mathcal{G}$ is decreased during the course of an experiment while in the strong flow regime, stability of the strong flow solution could be lost at a value other than $\mathcal{G}^*$, forcing a transition to the weak flow regime. A linear stability analysis of both solution branches is required to ascertain the parameter ranges in which each solution is stable, and to predict any possible hysteresis in the system as the flow rate is slowly increased or decreased.

Related to these considerations, we note that during our numerical investigations, a third solution branch was found, by imposing boundary condition $\theta(-1) = \pi$ in place of the condition $\theta(-1) = -\pi$ in (8). This solution branch, an example of which is shown in Fig. 6, is clearly energetically unfavorable; the boundary conditions are forcing the director to rotate through an angle $+\pi$ across the channel width, but the flow near the walls acts to push the director in the opposite (negative $\theta$) direction. The velocity

**Fig. 5.** Critical pressure gradient $\mathcal{G}^*$ at which transition from weak flow (anchoring-dominated) to strong flow solution is anticipated, as a function of dimensionless surface anchoring strength $\mathcal{A}$. Clearly, for small to moderate values of $\mathcal{A}$, there is a strong influence on $\mathcal{G}^*$.

**Fig. 6.** A third solution that we find when imposing boundary conditions $\theta(1) = 0$, $\theta(-1) = \pi$ (strong anchoring): (a) shows the director orientation within the layer, and (b) the velocity profile. Here, as in previous simulations, $\mathcal{G} = 25$. With an appropriate initial guess the analogous weak anchoring solutions may also be found.

profile is strongly peaked at the channel center. Variants on this solution can also (with an appropriate initial guess in the boundary value solver) be found when anchoring is weak. (We computed the energy of this solution branch; except at $\mathcal{G} = 0$ where it coincides with our strong flow solution branch, its energy is everywhere higher than both weak and strong flow branches.)

Fourthly, in making our comparison we are required to map between our dimensionless pressure gradient $\mathcal{G}$, which arises naturally in the model as a constant of integration, and the average flow speed $\bar{u}$, which was measured in the experiments. The expression (11) used for this estimate is based on the solution for Newtonian Poiseuille flow, which has the advantage of providing a simple comparison criterion, but which does not yield the same quantitative result as the averaged velocity for the nematic flow. Indeed, the averaged flow velocity for the nematic depends on which solution is considered: Figs. 1 and 4 reveal that the weak flow solution has always a lower averaged velocity $\bar{u}$ than the strong flow solution: $\bar{u}_{\text{weak flow}} < \bar{u}_{\text{strong flow}}$, for the same value of $\mathcal{G}$. Unlike in Newtonian flow, due to the different effective viscosities of the two director profiles, there is no one-to-one mapping between pressure gradient and flux: the same pressure gradient yields two solutions with different fluxes.

Our argument about the transition occurring at a certain value of the pressure gradient $\mathcal{G}$ is still sound, and we believe that the estimate given above, for the range within which the transition value of $\mathcal{G}$ should lie, is reasonable for a strictly two-dimensional flow. Nonetheless, the above observation raises the question: what is the exact transition value of $\bar{u}$, if this is the experimental control variable? Our results indicate that the same flow rate can be achieved at two different pressure gradients, indicating that the answer to this question should depend on the experimental protocol, which is not described in detail by Sengupta et al. [9]. Different protocols could give rise to different transition values of $\bar{u}$, as we now explain.

One possible protocol is that the microfluidic is filled with NLC, which is initially stationary. The driving pressure gradient is gradually increased, with observations made at regular pressure increments. In this situation we would expect the transition to occur at a value $\mathcal{G}^*$ obtained (within our simple modeling assumptions) as described in Section 3. As the transition occurs, the flow rate would jump from $\bar{u}_{\text{weak flow}}$ to $\bar{u}_{\text{strong flow}}$ (a larger value); the measured flow rate at transition would then be $\bar{u}_{\text{strong flow}}$.

A second possible protocol is that the microfluidic is started at a high flow rate, so that the system is initially in the strong flow regime with the director aligned with the flow. If the flow rate is then gradually decreased by lowering the applied pressure then again the transition would occur at the predicted value of $\mathcal{G}^*$, at which point the flow rate would jump from $\bar{u}_{\text{strong flow}}$ to $\bar{u}_{\text{weak flow}}$ (a smaller value); the measured flow rate at transition would then be $\bar{u}_{\text{weak flow}}$.

These simple arguments demonstrate that the details of the experimental protocol may be important in making a direct comparison to theoretical models.

## Acknowledgments

## Appendix A. Leslie–Ericksen model for nematodynamics

The full equations of nematodynamics describe the evolution of the director field $\boldsymbol{n} = (n_1, n_2, n_3)$ and the velocity field $\boldsymbol{v} = (v_1, v_2, v_3)$ as follows:

$$\lambda n_i - \partial W \partial n_i + \left(\frac{\partial W}{n_{i,j}}\right)_j + G_i = 0, \tag{12}$$

$$-\frac{\partial \Pi}{x_i} + G_k \frac{\partial n_k}{x_i} + \frac{\partial t_{ij}}{x_j} = 0, \tag{13}$$

$$\frac{\partial v_i}{\partial x_i} = 0 \tag{14}$$

representing energy, momentum and mass conservation, respectively. Here, $\lambda$ is a Lagrange multiplier ensuring that the director $\boldsymbol{n}$ is a unit vector. The quantities $W$, $G$ and $\Pi$ are defined by

$$2W = K\left((\nabla \cdot \boldsymbol{n})^2 + |\nabla \wedge \boldsymbol{n}|^2\right); \tag{15}$$

$$G_i = -\gamma_1 N_i - \gamma_2 e_{ik} n_k, \quad e_{ij} = \frac{1}{2}\left(\frac{\partial v_i}{\partial x_j} + \frac{\partial v_j}{\partial x_i}\right); \tag{16}$$

$$N_i = \dot{n}_i - \omega_{ik} n_k, \quad \omega_{ij} = \frac{1}{2}\left(\frac{\partial v_i}{\partial x_j} - \frac{\partial v_j}{\partial x_i}\right); \tag{17}$$

$$\Pi = p + W + \psi_g, \tag{18}$$

where $K$ is an elastic constant (this form of $W$ (15) exploits the widely used one-constant approximation [3]), $\gamma_1$ and $\gamma_2$ are constant viscosities; an over-dot denotes a material (total) time derivative; $p$ is the pressure and $\psi_g$ is the gravitational potential. Finally, $t_{ij}$ is the viscous stress tensor, given by

$$t_{ij} = \alpha_1 n_k n_p e_{kp} n_i n_j + \alpha_2 N_i n_j + \alpha_3 N_j n_i + \alpha_4 e_{ij} + \alpha_5 e_{ik} n_k n_j + \alpha_6 e_{jk} n_k n_i, \tag{19}$$

where $\alpha_i$ are constant viscosities (related to $\gamma_i$ in Eq. (16) by $\gamma_1 = \alpha_3 - \alpha_2$, $\gamma_2 = \alpha_6 - \alpha_5$, and to each other by the Onsager relation, $\alpha_2 + \alpha_3 = \alpha_6 - \alpha_5$).

## Appendix B. Parameter values for 5CB

For the liquid crystal 5CB (used by Sengupta et al. [9]) in the nematic state at $27\,°C$, the values for the viscosities [5,10] are $\alpha_1 = -0.011$, $\alpha_2 = -0.07$, $\alpha_3 = -0.0038$, $\alpha_4 = 0.071$, $\alpha_5 = 0.052$, $\alpha_6 = -0.028$ (all in Pa s, or $kg\,m^{-1}\,s^{-1}$, the SI units of viscosity), with other viscosity coefficients $\gamma_1 = \alpha_3 - \alpha_2$, $\gamma_2 = \alpha_6 - \alpha_5$. Dimensionless equivalents are obtained by normalizing each value with $\alpha_4$. The elastic constants for 5CB are approximately $K_1 = 4 \times 10^{-12}$ N (splay) or $K_3 = 4.8 \times 10^{-12}$ N (bend) [12].

## References

[1] L.M. Blinov, A.Yu. Kabayenkov, A.A. Sonin, Invited lecture: experimental studies of the anchoring energy of nematic liquid crystals, Liquid Cryst. 5 (2) (1989) 645–661.

[2] S. Chandrasekhar, Liquid Crystals, 2nd ed., Cambridge University Press, Cambridge, 1992.

[3] P.G. De Gennes, J. Prost, The Physics of Liquid Crystals, 2nd ed., International Series of Monographs on Physics, vol. 83, Oxford Science Publications, Oxford, 1995.

[4] A.H. Lewis, I. Garlea, J. Alvarado, O.J. Dammone, P.D. Howell, A. Majumdar, B.M. Mulder, M.P. Lettinga, G.H. Koenderink, D.G.A.L. Aarts, Colloidal liquid crystals in rectangular confinement: theory & experiment, Soft Matter 10 (40) (2014) 7865–7873.

[5] M. Inoue, K. Yoshine, H. Moritake, K. Toda, Evaluation of nematic liquid crystal director orientation using shear horizontal wave propagation, J. Appl. Phys. 91 (2002) 2798–2802.

[7] F.M. Leslie, Theory of flow phenomena in liquid crystals, Adv. Liquid Cryst. 4 (1979) 1–81.

[8] A. Rapini, M. Papoular, Distorsion d'une lamelle nématique sous champ magnetique. Conditions d'ancrage aux parois, J. Phys. Colloq. C4 30 (1969) 54–56.

[9] A. Sengupta, U. Tkalec, M. Ravnik, J. Yeomans, C. Bahr, S. Herminghaus, Liquid crystal microfluidics for tunable flow shaping, Phys. Rev. Lett. 110 (2013) 048303.

[10] K. Skarp, S.T. Lagerwall, B. Stebler, Measurements of hydrodynamic parameters for nematic 5CB, Mol. Cryst. Liquid Cryst. 60 (1980) 215–236.

[11] I.W. Stewart, The Static and Dynamic Continuum Theory of Liquid Crystals: A Mathematical Introduction, Taylor & Francis, London, 2004.

[12] P. Yeh, C. Gu, Optics of Liquid Crystal Displays, 2nd ed., Wiley, Hoboken, 2010.